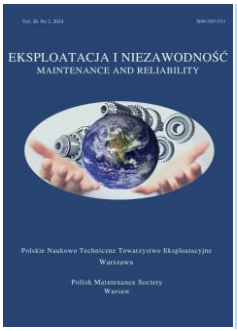

Eksploatacja i Niezawodnosc – Maintenance and Reliability

Volume 26 (2024), Issue 2

journal homepage: http://www.ein.org.pl

Article citation info:
Winnicki M, Łapa W, Świadkowski B, A novel approach to improve reliability of aerosol jet printing process, Eksploatacja i Niezawodnosc – Maintenance and Reliability 2024: 26(2) http://doi.org/10.17531/ein/180012

A novel approach to improve reliability of aerosol jet printing process

Indexed by:

Marcin Winnicki[a,*], Wojciech Łapa[a], Bartosz Świadkowski[b]

[a] Wroclaw University of Science and Technology Faculty of Mechanical Engineering, Poland
[b] Faculty of Electronics, Photonics and Microsystems, Wroclaw University of Science and Technology, Poland

Highlights

- 3D structures were aerosol jet printed using silver nanoparticles in a single-step.
- The intensive solvent evaporation caused local open porosity in non-heated samples.
- Fine droplets with diameter below 1 μm are ejected from the stream and spatter the foil.
- Concentration of nanoparticles was improved and defects limited due to in-line heating.
- IR sintering provided reduced nanoroughness and improved bonding of aggregates.

Abstract

Additive manufacturing is gaining interest for printing of noble metals. In this study, aerosol jet printing was applied to fabricate traces from commercial silver nanoparticle ink. A self-built three dimensional printing machine was used without or with in-line substrate heating. A conductive traces were printed on flexible polyimide substrates. Subsequently, sintering was conducted by furnace or near-infrared source. Examination of the sample using scanning electron and atomic force microscopy revealed the existence of both micro- and nanoscale pores in the structure. Local open porosity, aerosol extensive spatter and wide porous overspray were key defects found in samples printed without substrate heating. All the features affect the properties and reliability of silver prints. In-line process heating increased the concentration of nanoparticles and limited defects formation. What is more, the width of traces decreased from 31 μm to 19 μm with simultaneous thickness increase from 1.2 to 5.5 μm due to substrate heating. The final structure was influenced by sintering method and its time. Elongated time of sintering decreased porosity and roughness of the printed traces. Nevertheless, IR sintering provided the smoothest sample surface with lowest Sa roughness of 16 nm, and significantly improved bonding of aggregates. What is more, the printed structure had a measured sheet resistance of 8.3×10^{-2} Ω/□.

Keywords
printed flexible electronics, polymer substrate, aerosol stream, silver traces, overspray, sheet resistance

1. Introduction

Printed flexible electronics (PFE) was developed to overcome the limitation of rigid and brittle traditional electronics by the use of elastic materials to fabricate electronic circuits that can be stretched or bent without breaking while still maintaining desired electronic properties. This technology is being used in a wide range of applications, including smart packaging, sensors [8], displays, and energy harvesting [60], [33], that are lightweight, low cost, and can be easily integrated into a range of electronic devices. The manufacture of flexible, stretchable, wearable, and conformal electronic components is possible due to several conventional, 3D, and hybrid printing technologies, where the most popular are: (i) inkjet printing [20], [2], (ii) aerosol jet printing [12], [58], (iii) screen printing [37], [68], (iv) gravure printing [48], [47], or (v) stereolithography [38], [39].

(*) Corresponding author.
E-mail addresses: M. Winnicki (ORCID: 0000-0003-2766-116X) marcin.winnicki@pwr.edu.pl, W. Łapa (ORCID: 0000-0002-3434-865X) wojciech.lapa@pwr.edu.pl, B. Świadkowski (ORCID: 0000-0001-9197-1862) bartosz.swiadkowski@pwr.edu.pl,

Among these, inkjet printing (IJP) and aerosol jet printing (AJP) are recently developed due to capability of printing at high resolution with less material wastage and comparably low electrical resistivity of c.a. 4.5×10^{-8} Ωm (~3 × bulk Ag) [66]. While IJP is dedicated for flat 2D surfaces, AJP can be applied to print on 3D objects. AJP utilizes an aerosol stream generated from metal nanoparticle-based conductive inks to deposit small droplets of material onto a substrate. A mean size of metal nanoparticles in the ink is usually c.a. 10 nm [62] or 50-60 nm [35].

The AJP process has the capability of direct writing and works without conventional masks, due to easy control and selective deposition of inks at precisely defined locations on the substrate. High resolution ensures the fabrication of prints as small as a few micrometres in size [22] with a high level of precision and accuracy, while high printing speeds make the process a suitable technique for high-volume production applications. A commercially available printers enable fabrication patterns with a minimum feature size starting from 15 μm up to few cm in width and 0.1 μm in thickness [55]. The versatility to apply a wide range of materials results from an atomiser used to create a dense aerosol of microdroplets focused by shielding gas in an aerosol stream [13]. Unlike other printing techniques, AJP operates without physical contact between the printing head and the flexible substrate and allows printing on uneven or curved surfaces. The geometry of printed paths, e.g. width and high, is regulated by nozzle outlet orifice diameter and stand-off distance. Furthermore, compared to traditional approaches, aerosol reduces the cost of ink consumption and limits the waste of hazardous materials used in the etching processes employed by subtractive methods. These features multiply the applications of the AJP process in the fabrication of high-quality devices. However, AJP prints show the same problems as IJP, e.g. micro- and nanoscale pores within the structure, which significantly affect the properties and reliability of PFE. While in IJP the key factors contributing to the voids are usually the pinning effect, residual surface temperature, insufficient droplet overlap and surface defects [64], in AJP it is the diameter of the aerosol droplets and surface temperature [34]. What is more, the challenging issue in the AJP is the selection of parameters to avoid overspray formation. Overspray refers to the unintended dispersion and scattering of the aerosol, which is deposited in the peripheral region of the trace and deteriorates its reliability. As small droplets with low inertia contribute mainly to overspray, there are several factors that maximise homogeneity of the printed path, including nozzle design, aerosol generation method, ink properties, gas pressure, and substrate characteristics [42],[67],[57].

The substrate materials used in PFE are typically polymers or other organic materials that have some degree of elasticity, chosen for their mechanical properties, including flexibility, stretchability, and durability. Some of the substrate materials used in PFE include: (i) polyimide (PI) [1]; (ii) polyethylene terephthalate (PET) [46]; (iii) polydimethylsiloxane (PDMS) [10]; (iv) polyvinyl chloride (PVC) [36] or (v) paper [36]. However, flexible substrates need to withstand the high temperature during processing and match the coefficient of thermal expansion (CTE) of the deposited material. It should be noted that PI, among others, shows excellent heat resistance and dimensional stability, i.e., glass transition temperature (Tg) >450 ˚C and CTE at 0 – 10 ppm·K^{-1} [11],[24]. Additionally, PI have mechanical properties to ensure the service life of the device after multiple bending [25]. Therefore, in PFE fabrication, which include high-temperature sintering, PI is commonly applied.

The printing process leaves semi-wet paths of ink on the surface of flexible polymer substrate [65]. However, to transform the printed layer into a conductive one, a sintering procedure is necessary to evaporate the solvent, remove the polymer capping shell, and join the metal nanoparticles (NPs). It is worth mentioning that nanometer size of the metal particle significantly lowers the sintering temperature compared to bulk material. Nevertheless, in conventional furnace sintering, a temperature of c.a. 200 ˚C for a minimum of 30 min is required [58]. Some authors combined chemical and thermal sintering [23], however ink composition should be considered. To improve the process and eliminate substrate material limitations, other sintering techniques are proposed, e.g. electrical [6], photonic [31] or microwave [9]. Due to processing speed, simplicity and prints quality, photonic sintering [43] is more and more popular, with the following radiation sources: laser [3],[49], flash lamp [31], UV lamp [53],[51] or IR lamp [28],[61]. Photonic sintering aims to achieve targets rather than heating the entire system indiscriminately. In consequence,

conductive paths absorb the radiation, leaving the polymer substrate usually unaffected. The absorption spectra of silver NPs can vary depending on their size, shape, or composition. Nevertheless, for spherical silver NPs, the absorption peak is typically in the range of 400-450 nanometres [14], [15]. Therefore, the application of UV light with wavelength ranging from 100 to 400 nm is limited [43], while laser depending on optical properties of the ink and the absorption characteristic of the NPs, have to be designed for dedicated application [56]. Although flash lamps are very popular, intense pulse lights (IPL) and its wide spectra that embrace UV, visible and near-IR regions, irradiate on the polymer surface, limiting the application of the selected substrate materials [27]. In this case, the IR lamp becomes very promising in PFE sintering. IR technology uses irradiation in the near infrared (750 to 2,500 nm) and provides selective heating and short time sintering of printed metallic NPs [28].

Printed electronics often involves complex patterns and structures with varying geometries, such as lines [22], dots, and interconnections [54]. Achieving consistent and uniform printing quality across the entire substrate can be difficult due to factors such as ink flow, substrate roughness, and ink-substrate interactions. Variations in ink viscosity, surface tension, and drying characteristics can lead to defects and inconsistencies in printed structures. The quality assessment of the silver NPs-based printed electronics is complicated due to complexity of the fabrication process (e.g. ink preparation, printing, drying, curing, and post-processing) and small size of the prints as well as applied metallic powder. The crucial factor characterising the prints is electrical conductivity, which is influenced by the packability of silver NPs and sintering. Good packability is defined as high density of metal NPs [71], while sintering refers to the removal of chemical agents and the joining of NPs to establish a conductive network [40].

PFE is a rapidly evolving field, and standardised testing methods for quality assessment are still being developed. There may be a lack of universally accepted protocols and techniques for evaluating critical parameters such as electrical conductivity, mechanical properties, and the durability of printed structures. As a consequence, it is difficult to compare results across different studies. Therefore, within the proposed paper, Ag NP based ink was applied in the AJP process to fabricate prints on thin and flexible polyimide substrates. Samples were prepared with or without additional in-line substrate heating. Two types of sintering methods were used, the furnace and the infrared lamp. Printed samples were scanned and analysed with the use of various types of microscopes, e.g., light microscope (LM), scanning electron microscope (SEM), confocal microscope (CM), and atomic force microscope (AFM). Samples with significant morphological and structural differences were produced due to different process parameters configurations. Finally, the fabrication techniques were summarised, and optimal parameters were selected to improve the structure and reliability of printed traces.

2. Materials and methods

2.1. Aerosol jet printing process

In the research a self-built aerosol jet printer was used. The setup with the operating principle of the printing process is presented in Fig. 1.

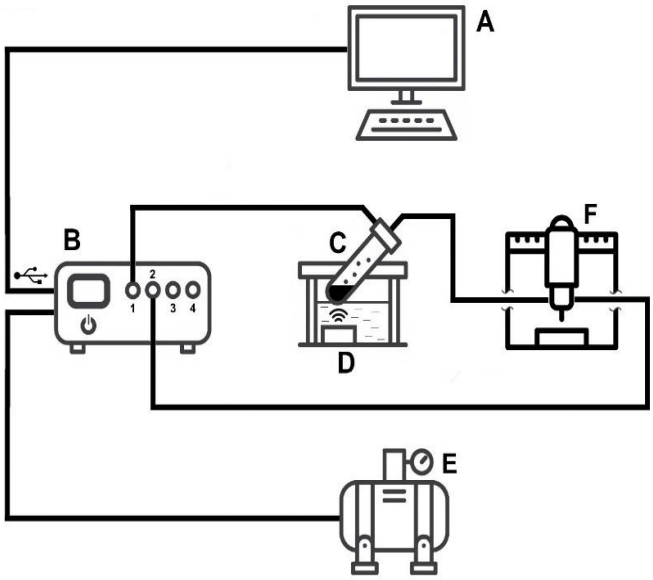

Fig. 1. Schematic diagram of the aerosol jet printer with an ultrasonic atomiser equipped with: A – control unit, B – microfluidic flow controller, C - ink reservoir, D – ultrasonic generator, E – air compressor and F – printing head with the nozzle fixed above moving bed

An aerosol was generated by an ultrasonic transducer working with a frequency of 1.7 MHz and a power of 18 or 24 W in a reservoir filled with 5 ml of suspension, which was conductive ink. The size of generated aerosol droplets was mostly in the range of 8-17 μm [34]. Produced aerosol was

transported to the printing head by compressed air, which was used as aerosol carrier and sheath gas. After being compressed and accelerated by a sheath gas stream, the flowing ink aerosol was sprayed out of the nozzle through an orifice with an inner diameter of 0.36 mm to form thin conductive traces on the foil substrate. The printing head was attached to the manipulator arm with a stand-off distance of 3 mm above the bed (Fig. 2). A microfluidic flow controller (Elveflow OB1 MK3+, Paris, France) enabled precise regulation of compressed air pressure down to 1 mbar. Samples 15x60 mm made of polyimide foil 100 µm thick (previously degreased with ethanol) were fixed to the high-precision mobile CNC heating bed with magnets. A length of printed traces was 50 mm. The selected samples were printed with additional in-line heating of the substrate material at a temperature of 90 ˚C.

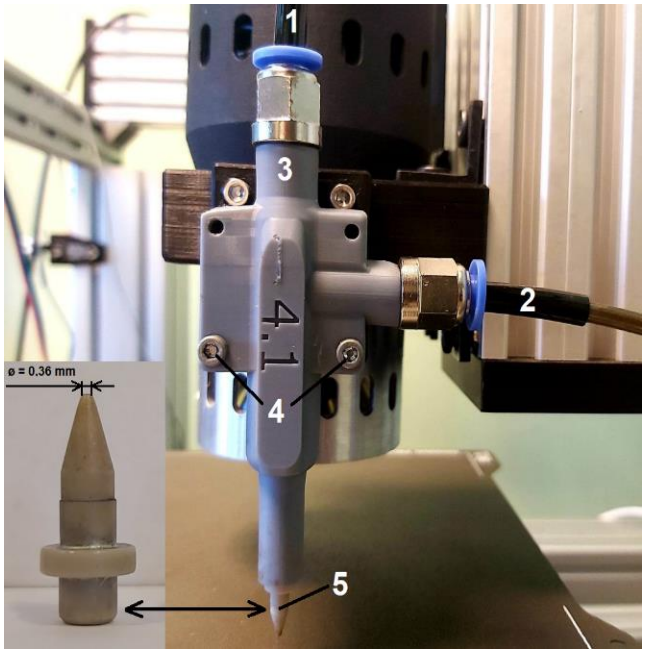

Fig. 2. Printing head (front - A) and IR lamp (back - B) fixed in the holder and attached to manipulator arm, C – heating and moving bed. 1 – aerosol inlet, 2 – shielding gas inlet, 3 – main resin-printed body, 4 – fixing screws, 5 – exchangeable nozzle with inner orifice diameter of 0.36 mm.

The ink used in the research is a commercially available suspension of silver nanoparticles (d_{50} = 6 nm up to 45 vol.%) suspended in solvent, mostly tetradecane or a mixture of ethanol and glycol (Amepox Microelectronics, Ltd., Łódź, Poland). Properties of the ink are collected in Tab.1. The research was divided into two stages: (1) printing parameters selection, i.e., pressure of carrier and sheath gas; and (2) printing and sintering of traces with selected parameters and various drying and sintering options. The printing process parameters applied in stage (1) are collected in Tab. 2. It should be emphasised that smaller pressure of carrier gas (CG) and sheath gas (SG) enables precise control of the printing process with limited ink waste. What is more, preliminary studies showed that the printing process is stable without nozzle clogging or aerosol stream choking with the SG in the range of 120-360 mbar. Therefore, the pressure of SG in this study was selected to 240 mbar. The printing velocity in both stages was set to 73 mm/min. The printing was performed with control room temperature of 22 ˚C and humidity of 50%.

Table 1. Properties of the utilized ink provided by manufacturer [73].

Dynamic viscosity [m·Pa·s]	Surface tension [dynes/cm]	Density [g/cm^3]	Silver content [%]	Silver powder particles size range [nm]
7.5-10.5	28.5-32.5	1.1-1.3	45	3-8

Table 2. Range of printing parameters in stage (1).

Pressure of aerosol carrier gas (mbar)	Pressure of sheath gas (mbar)	Number of layers
40; 60; 80	240	1

Two types of conducting ink sintering were applied: (i) conventional furnace sintering at 230 ˚C for 60 min or 120 min and (ii) IR lamp sintering with voltage of 5 V (50% of the maximum power), four passes with traverse velocity of 10 or 20 mm/min. The ink manufacturer suggests sintering in the furnace sintering for 60 min. Printed traces were analysed at different variations of sample preparation: (i) as printed without a heating table, (ii) as printed with a heating table, (iii) as printed with or without a heating table and sintered in a furnace, and (iv) as printed with or without heating table and sintered by IR lamp. The samples were sintered in a muffle furnace (Nabertherm LT9/12, Lilienthal, Germany) with a heating temperature range of 30-1300 ˚C and by infrared adphosNIR dot lamp (adphos, Bruckmuehler, Germany) equipped with a 150W emitter halogen lamp. A dedicated head focusses NIR (near infrared) light to a small heated area with a diameter of around 7 mm providing a high heating energy density of 3.9 W/mm^2. The system heats only a very small round area and thus needs transport during operation. The precise specification and process parameters of printing and post-printing treatment are collected and presented in Tab. 3.

Table 3. Parameters of sintering in stage (2).

Sample description	Notation	Temperature of heating bed [˚C]	Furnace heating time [min]	IR lamp voltage [V]	Traverse velocity [mm/min]
As – printed	AP	-	-	-	-
As – printed with bed heating	AP+H	90	-	-	-
Furnace sintering 1	FS 1	-	60	-	-
Furnace sintering 2	FS 2		120	-	-
Furnace sintering 1 – AP with bed heating	FS 1 + H	90	60	-	-
Furnace sintering 2 – AP with bed heating	FS 2 + H	90	120	-	-
IR lamp sintering 1	IR 1	-	-	5	10
IR lamp sintering 2	IR 2	-	-	5	20
IR lamp sintering – AP with bed heating 1	IR 1 + H	90	-	5	10
IR lamp sintering – AP with bed heating 2	IR 2 + H	90	-	5	20

* AP – as - printed

2.2. Printed traces characterization methods

The microscope analysis of printed and sintered traces was performed using VHX-6000 digital microscope - DM (Keyence VHX-6000, Osaka, Japan) and the atomic force microscope – AFM microscope (NT-MDT NTEGRA Prima, Apeldoorn, The Netherlands). AFM scans were performed with the use of resonant, noncontact mode, and NANOSENSORS PPP-NCLR cantilevers. Additionally, the surface of sintered traces was analysed with the use of scanning electron microscope - SEM (Tescan VEGA 3 SBH, Brno, Czech Republic) equipped with SE, BSE detectors, and EDS system for elemental analysis and confocal microscope – CM (Olympus Lext OLS5100). Surface morphology, dimensions, and overspray were assessed by DM and SEM, while CM and AFM provide surface topography parameters (profile high and roughness) and irregularity dimension. Linear roughness was measured on the axis of the trace line by CM, while square roughness was measured as a rectangle 20x50 μm by AFM. For the electrical characterizations, i.e. prints resistance, a 4-point probe measurement method with precise measure unit (B2901BL, Keysight Technologies, Santa Rosa, the USA) was used. A resistance measurements were performed on at least three randomly selected samples at constant temperature of 22 °C.

3. Results

3.1. Parameters selection

The research began with many experiments combining various process parameters. Parameter selection aimed to achieve homogeneous traces with width below 50 μm (excluding overspray) and regular and smooth surface. It is obvious that increasing the pressure of sheath gas results in a decrease of the printed trace width. However, the carrier gas (CG) and the sheath gas (SG) are mutually dependent. After exceeding the crucial pressure value of the SG, the aerosol will not be dosed without increasing the CG. On the other hand, high pressure of the CG will provide intensive aerosol deposition, resulting in a wide trace.

The smallest tested CG pressure of 40 mbar produced traces with a width of about 120 μm including overspray, which was difficult to distinguish due to irregular and rough surface (see Fig. 3a). Furthermore, intensive overspray is visible on the left and right sides of the path direction. It suggests that the aerosol cloud consisting of the finest droplets was formed and ejected from the printed stream by SG. Therefore, the aerosol cloud in form of spatter is responsible for the intense smudging of the foil. In the central part of the trace, the presence of agglomerated, chemically bonded particles, irregularly deposited on the

substrate, was confirmed by AFM measurements (Fig. 3b). Lateral and longitudinal scans with a confocal microscope showed open porosity in the central part of the trace (Fig. 4).

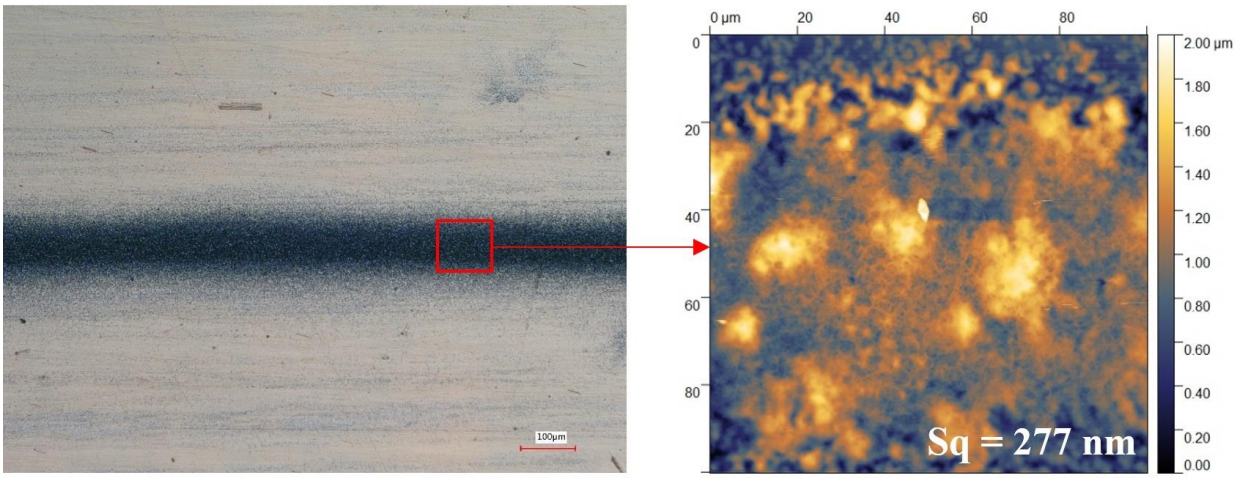

a) b)

Fig. 3. Micrographs of irregular trace printed with smallest CG of 40 mbar, DM (a) and AFM (b).

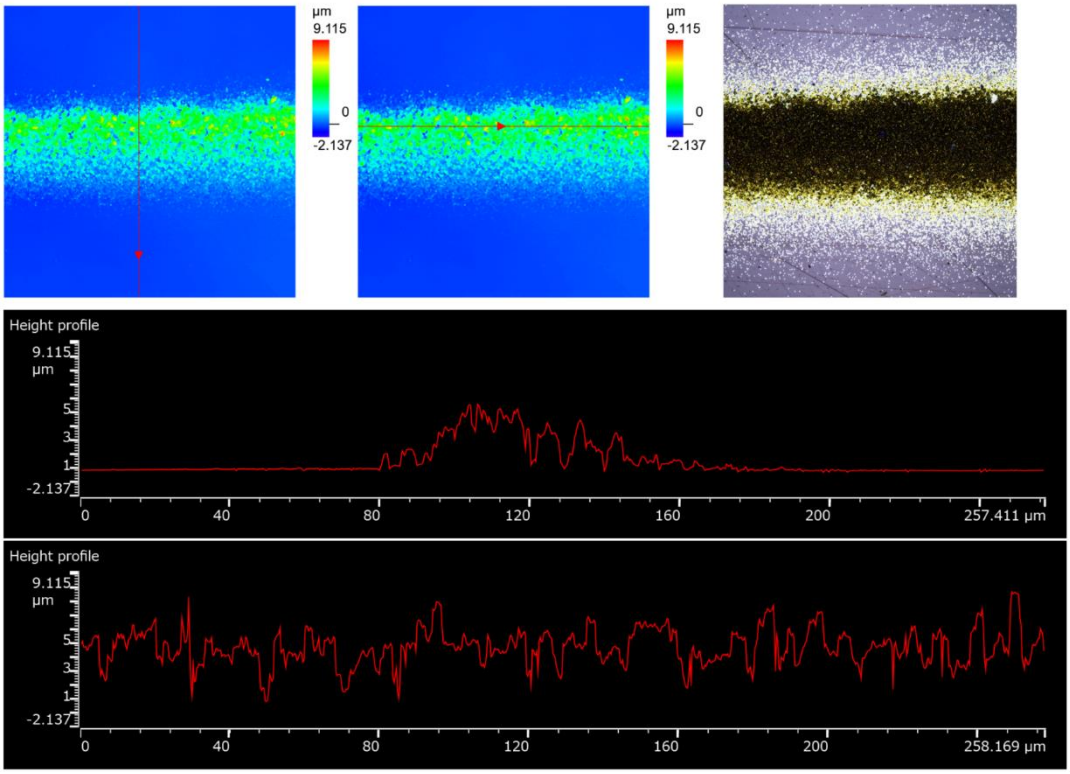

Fig. 4. CF scans of the sample presented in Fig. 3, profile directions (a,b), scanned surface (c) and generated lateral (d) and longitudinal (e) profiles.

When the parameter values were switched and the CG pressure of 60 mbar, the trace width was maintained the same. However, the structure of the trace changed significantly and consisted of two visible parts: (i) central homogeneous line with the width of 38 µm and line with peripheral overspray with the width c.a. 200 µm. It is worth stressing that aerosol cloud was significantly reduced. The higher pressure of the CG increased the amount of aerosol particles in the stream, as the well as proportion of fine to large particles. The central homogeneous line is smooth with only local pores (Fig. 5a). The highest tested pressure of 80 mbar provided the highest amount of aerosol to the stream and formed traces with the highest width in the range of 60-70 µm (central line) and above 200 µm (line with overspray). The overspray widening is proportional to the

growth of the trace volume. However, more fine particles were transported in aerosol cloud by higher pressure, causing intensive spatter on both sides of the trace (see red arrows in Fig. 5b). The central line is visibly homogeneous due to the increased amount of ink aerosol in the stream.

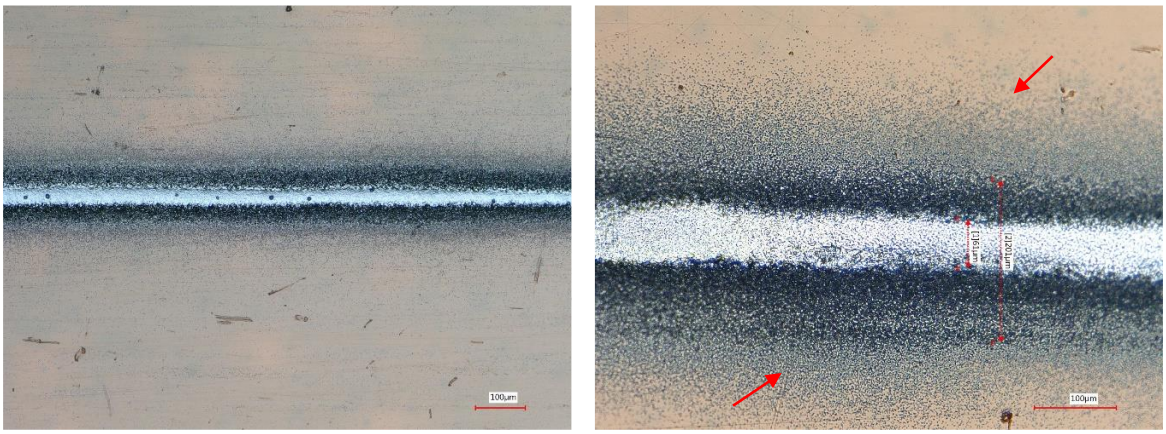

Fig. 5. Micrographs of trace printed with CG of 60 mbar, mag. 200x (a) and 80 mbar, mag. 500x (b), DM. Red arrows indicate spatter caused by aerosol cloud out of the trace path.

3.2. In-line drying effect

The results of printing process with selected in stage (1) optimal parameters (CG: 60 mbar) and without heating of the bed are presented in Fig. 6a. It is clearly visible that printed traces are well concentrated in the main axis. However, intensive spatter occurred, smudging all around the polymeric substrate. What is more, some local irregularity of the trace was found with significant open porosity in the central, thickest part of the trace (Fig. 6b). The porosity resulted from evaporation of the solvent. Samples were kept at room temperature and measured 1 h after deposition. In this short time the drying liquid transformed into gas and by the arising pressure was removed from the deposited material, leaving open porosities in the central continuous part of the prints resembling 'chimneys'.

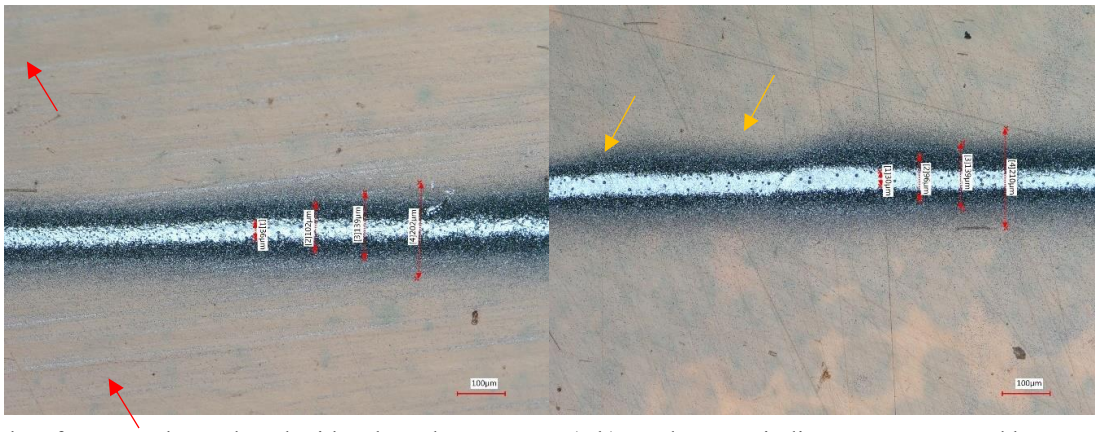

Fig. 6. DM micrographs of AP sample produced with selected parameters (a,b). Red arrows indicate spatter caused by aerosol cloud out of the trace path, while yellow arrows point irregularity of the trace - cyclical wider and narrower areas.

The application of heating significantly changed the print characteristic. Bed heating causes an increase of the process temperature, changing the flow characteristic and heterogeneity of the traces. It is stated that heated nozzle acts as capillary with rising pressure, which as a result increased velocity of the SG in the nozzle. What is more, the rising temperature affected the aerosol material as well. The intense evaporation of the liquid in the stream significantly increased the viscosity of the ink aerosol and initiated the agglomeration of the droplets. As a consequence, the deposited material forms a porous and rough structure, without spreading and filling a free space (see Fig. 7). The thickness of the path is c.a. 6 µm. However, due to extremally high longitudinal roughness (Ra = 0.52 µm and Rz = 3.93 µm), the trace has black colour. However, in the contrary to the samples printed with the lowest CG pressure in stage (1) and shown in Fig. 4, the trace was rather continuous just with

local open porosity (Fig. 7c).

Therefore, to solve the problem, the power of the ultrasonic generator was increased from 18 W to 24 W. The increased volume of aerosol generated in the reservoir prevented intensive evaporation of the liquid and production of completely continuous and smooth traces (Fig. 8). In this case, the longitudinal roughness was significantly decreased to Ra = 0.11 µm and Rz = 0.7 µm.

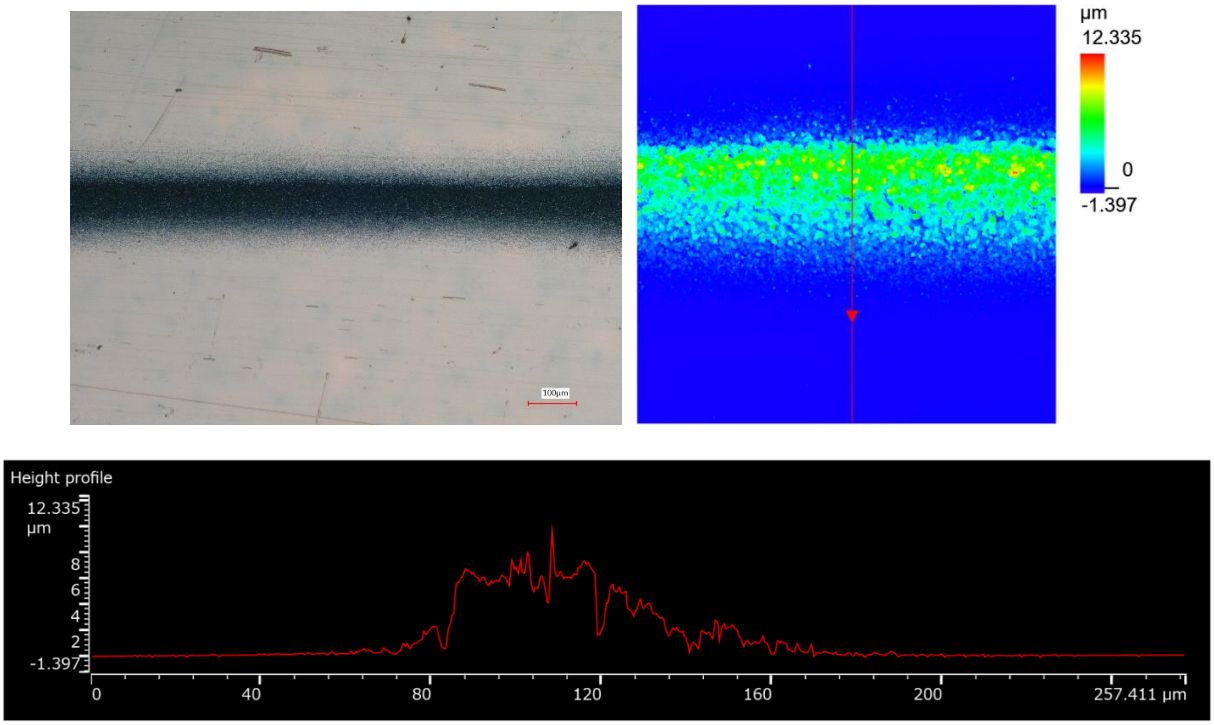

Fig. 7. Micrographs of rough trace printed onto heated substrate (AP+H) with insufficient aerosol volume, DM (a), CM (b) and lateral profile (c).

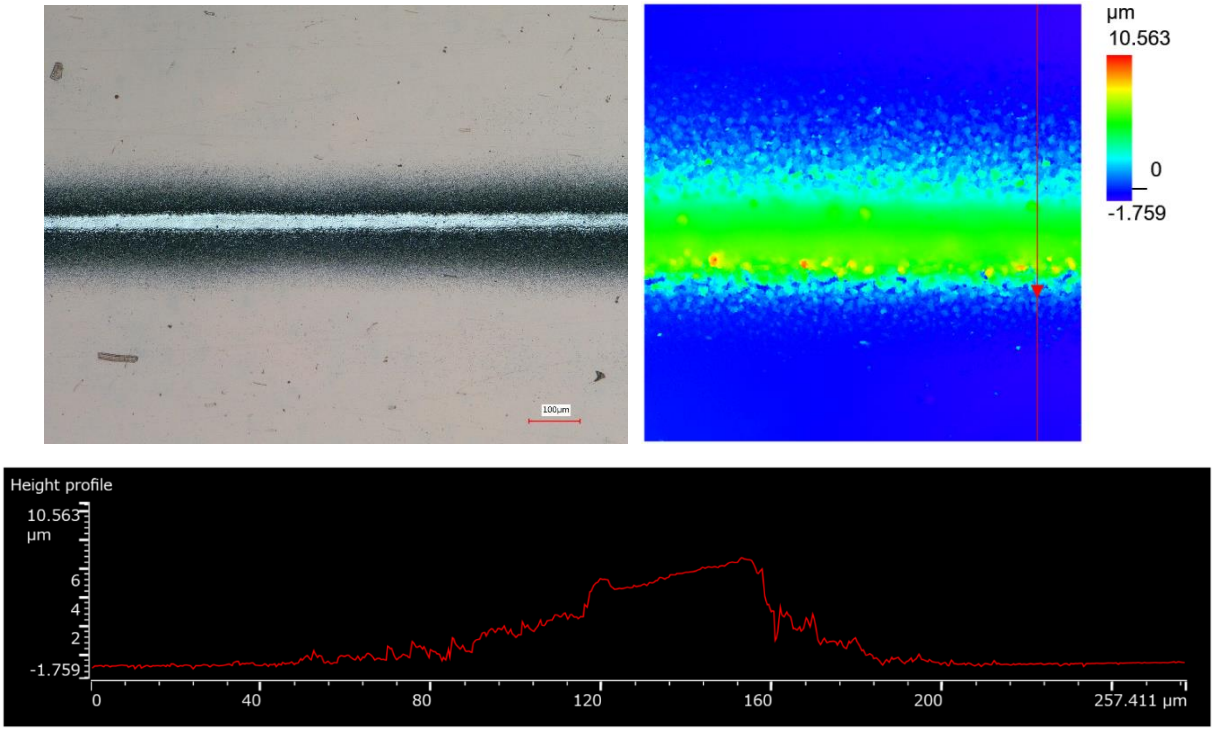

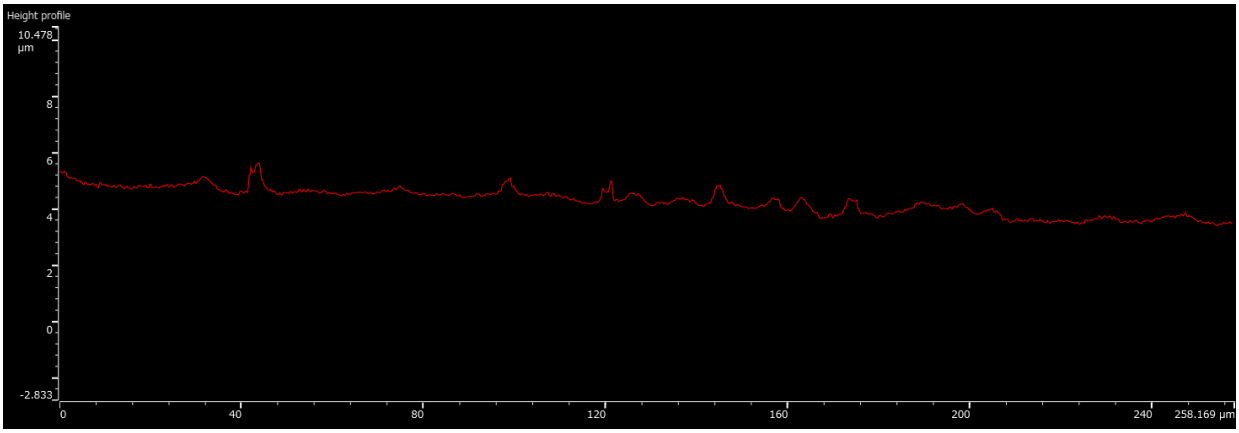

Fig. 8. Micrographs of smooth trace printed onto heated substrate (AP+H) with appropriate aerosol volume, DM (a), CM (b) and generated lateral (c) and longitudinal (d) profiles.

The results of printed traces geometry and surface parameters measurements are presented in Tab. 4. Despite spatter formation, all traces printed without substrate heating showed high width of the main body, as well as large overspray, in the range of 30-35 µm and 186-203 µm, respectively. On the contrary, samples prepared with additional heating showed width in the range of 19-23 µm. Furthermore, the thickness of the prints carried out with and without heating of the substrate foil was 5.5 µm and 1.2 µm, respectively. This huge difference arose from liquid evaporation and changed the viscosity of the ink aerosol by increasing the temperature. As a result, the overspray was limited, and an increase in thickness was noted. However, sintering caused the evaporation of liquid and polymer residues, which decreased the thickness of the traces. All samples showed low Ra and Rz roughness below 0,1 µm and 1 µm, respectively. Correlating the geometry of trace with resistance measurements, a sheet resistance of the prints was calculated (Tab. 4). It is clearly visible, that the highest sheet resistance up to 29.6 Ω/□ presents traces sintered in furnace for 1 h. Increasing the sintering time to 2 h decreased twice the order of magnitude. Further decrease provided NIR lamp sintering, while the lowest result of 0.083 Ω/□ was achieved for IR1+H sample.

Table 4. Selected parameters of printed traces.

Parameter	Sample No.									
	AP	AP+H	FS 1	FS 2	FS1+H	FS2+H	IR 1	IR 2	IR1+H	IR2+H
Mean trace width [µm]	31	19	32	35	23	21	32	30	20	21
Mean trace width with overspray [µm]	198 (SF)	137	194 (SF)	203 (SF)	127	135	186 (SF)	187 (SF)	148	139
Mean thickness [µm]	1.2	5.5	1.1	0.9	2.7	2.5	1.3	1.2	2.4	2.3
Profile max [µm]	2.5	10.6	2.1	2	5.5	5.2	2.1	2.2	5.7	4.9
Ra [µm]	0.09	0.1	0.06	0.08	0.07	0.05	0.04	0.07	0.05	0.05
Rz [µm]	0.66	0.7	0.4	0.53	0.51	0.94	0.36	1.13	0.37	0.66
Sheet resistance Rs [Ω/□]	N/A	N/A	29.6	0.283	11.8	0.230	0.116	0.143	0.083	0.088

* SF – spatter formation, described as extensive overspray covering substrate up to 3 mm on both sides of the trace

3.3. Furnace sintering

Aerosol jet printed traces require a post-printed sintering process to achieve optimal conductivity and mechanical integrity. The sint1ering process involves subjecting the printed traces to elevated temperatures, which promotes the bonding and consolidation of the conductive particles in the ink. The

basic method for sintering printed traces is furnace heating. Both types of samples, as-printed and as-printed with in-line heating, were sintered in furnace for 1 or 2 hours. Despite the manufacturer's suggestions for sintering time (1 hour) [73], we extended the time to 2 hours and compared the surface structure and prints properties. Extended time of samples curing in furnace should supply additional energy to silver nanoparticles and improve sintering process. The sintered samples showed the same features as the non-sintered samples. Therefore, samples produced without in-line heating (FS2) were characterized by intensive overspray and open porosity as well (Fig. 9a). On the contrary, the trace printed on a heated substrate (FS2+H) is centred, regular, and satisfactory narrow (Fig. 9b). The samples sintered in a furnace for 1 and 2 hours seemed to have a similar surface structure (Figs. 10 and 11). However, high resolution scans on AFM showed nano-porosity in sample sintered for 1 h (FS1) (Fig. 10b), while nano-roughness due to existence of nano-plateaus in sample sintered for 2 h (FS2) (Fig. 11b). As a result, the former sample had higher surface mean roughness Sa and Sq compared to the latter (Tab. 5).

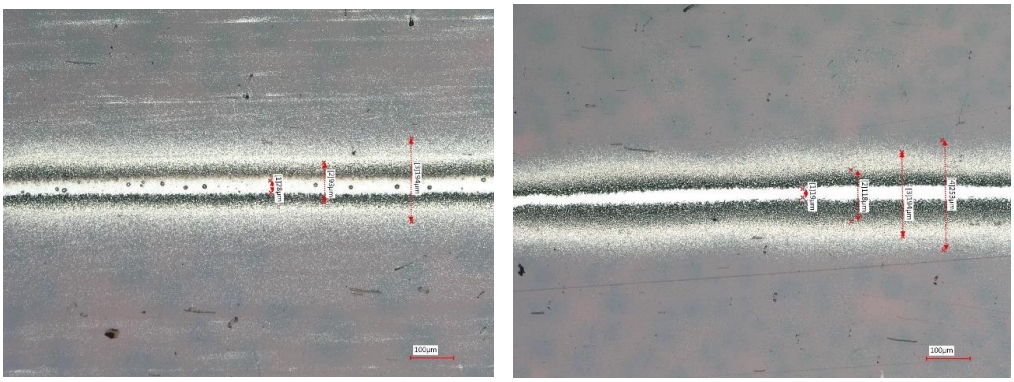

Fig. 9. DM micrographs of sample FS 2 (a) and FS 2 + H (b).

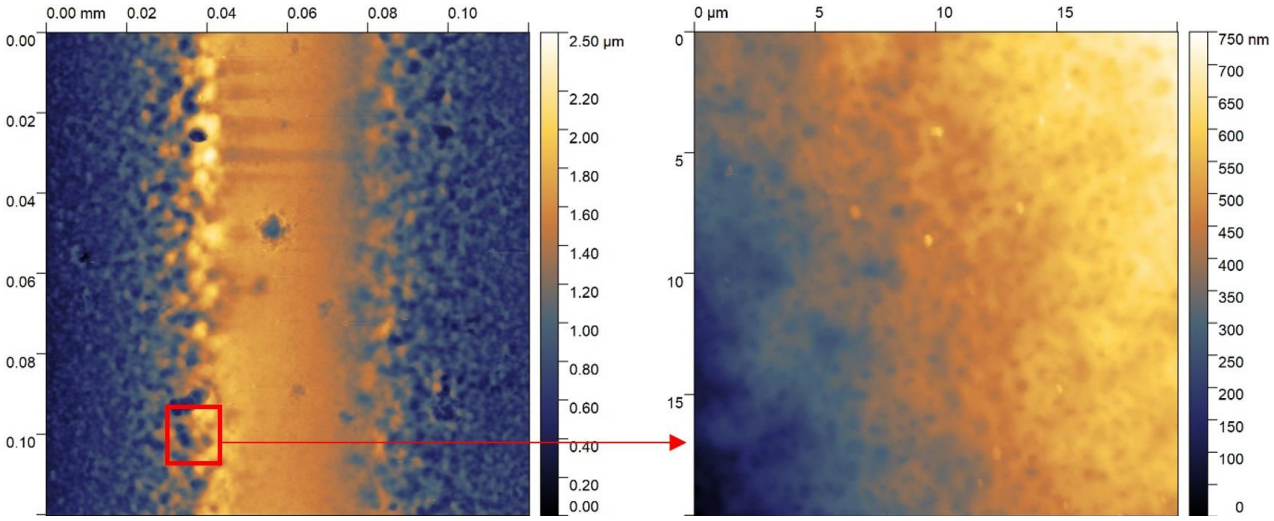

Fig. 10. AFM scans of sample FS 1 (a,b)

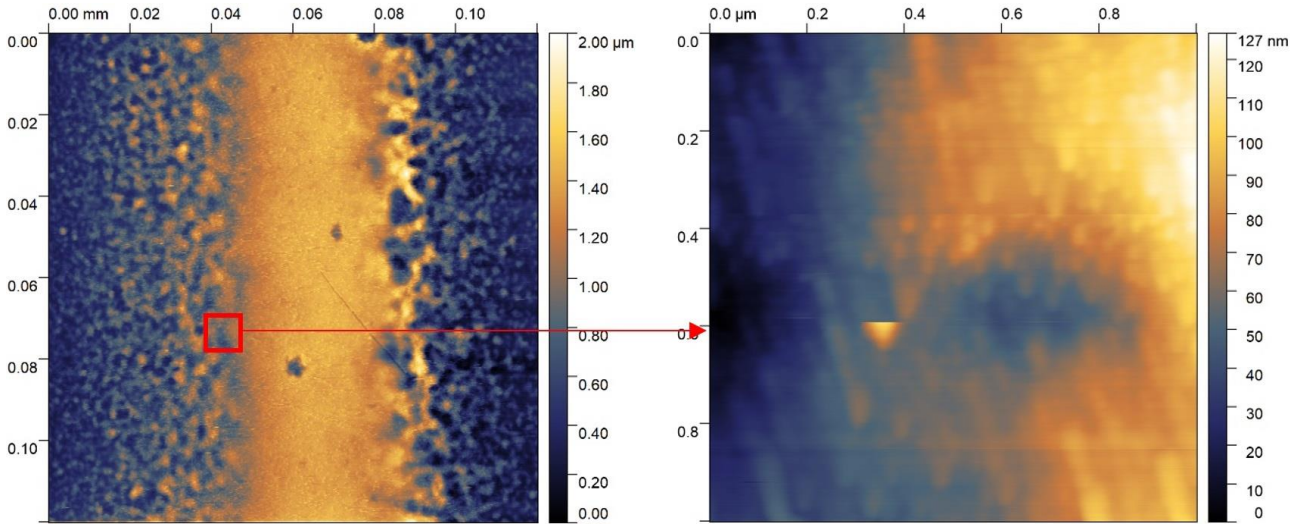

Fig. 11. AFM scans of sample FS 2 (a,b).

Table. 5. Nano-scale roughness of samples measured by AFM.

Parameters	Sample									
	AP	AP+H	FS1	FS2	FS1+H	FS2+H	IR1	IR2	IR1+H	IR2+H
Sa [nm]	N/A	821	110	63	142	127	16	52	61	128
Sq [nm]	N/A	932	135	79	182	157	21	63	77	149

Quite different appeared to be samples fabricated without (FS2) and with (FS2+H) in-line substrate heating and sintered in furnace for 2 hours. Nevertheless, the variations arose from printing process performance. A non-heated substrate sample showed intensive porosity in the form of locally present large open pores with diameter up to 8 µm and many small craters with diameter below 1.5 µm (see Fig. 12a). Despite those defects, the trace is continuous with an overspray having width of 20-25 µm on both sides. The substrate heating provides a sample free of porosity (Fig. 12b). However, the overspray region is intensively developed. An AFM scans confirmed high peaks in the trace/overspray boundary, known as the coffee ring effect (CRE) (Fig. 13). The increase in overspray height resulted from accelerated evaporation of liquid present in the ink aerosol and enhanced deposition of ejected droplets. The CRE is visible in the DM microscope as a black region (see Fig. 8 a and b, both sides of the traces). It should be emphasised that according to SEM results this region is discontinuous. To confirm this statement, an additional sample was printed with insufficient aerosol volume on heated substrate (the same as shown in Fig. 7) and sintered in furnace for 1 hour. The DM showed a potentially satisfactory trace with a black region in the middle (Fig. 14a), while the CM scan suggests intensive porosity in this region (Fig. 14b). The reliable result with spongy structure and discontinuity is provided by the SEM image (Fig. 14c). Therefore, DM and CM surface analysis can be misleading and should be confirmed by SEM or AFM scans.

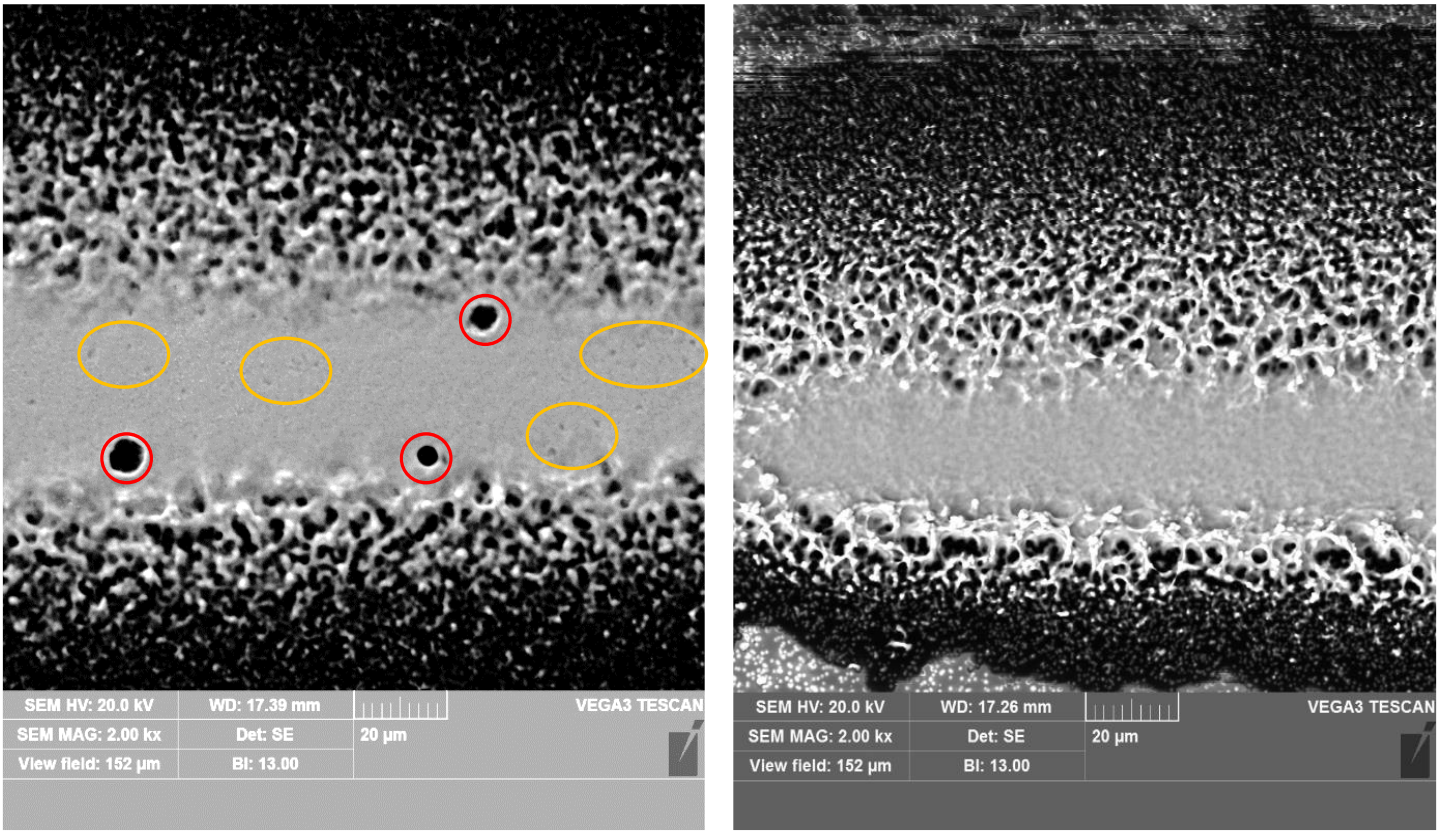

Fig. 12. SEM micrographs (SE) of sample FS 2 (a) and sample FS 2 + H (b). Red circles and yellow ellipses mark open porosity and small craters, respectively.

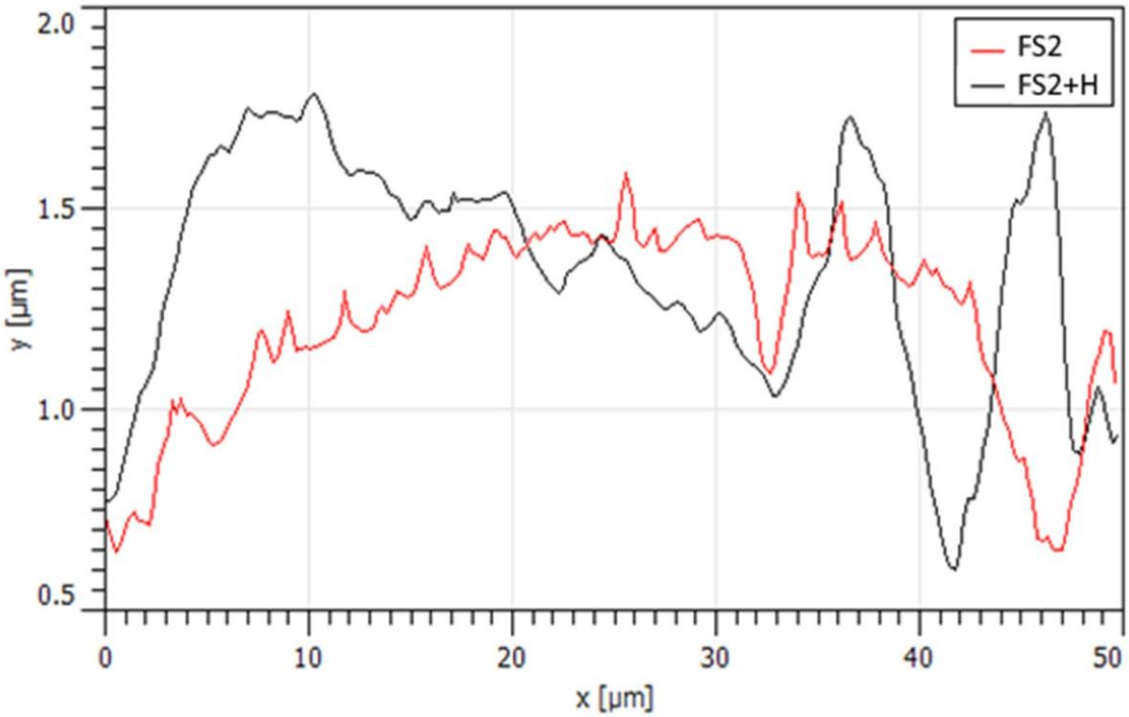

Fig. 13. AFM profiles of sample FS 2 (red profile) and FS 2 + H (black profile).

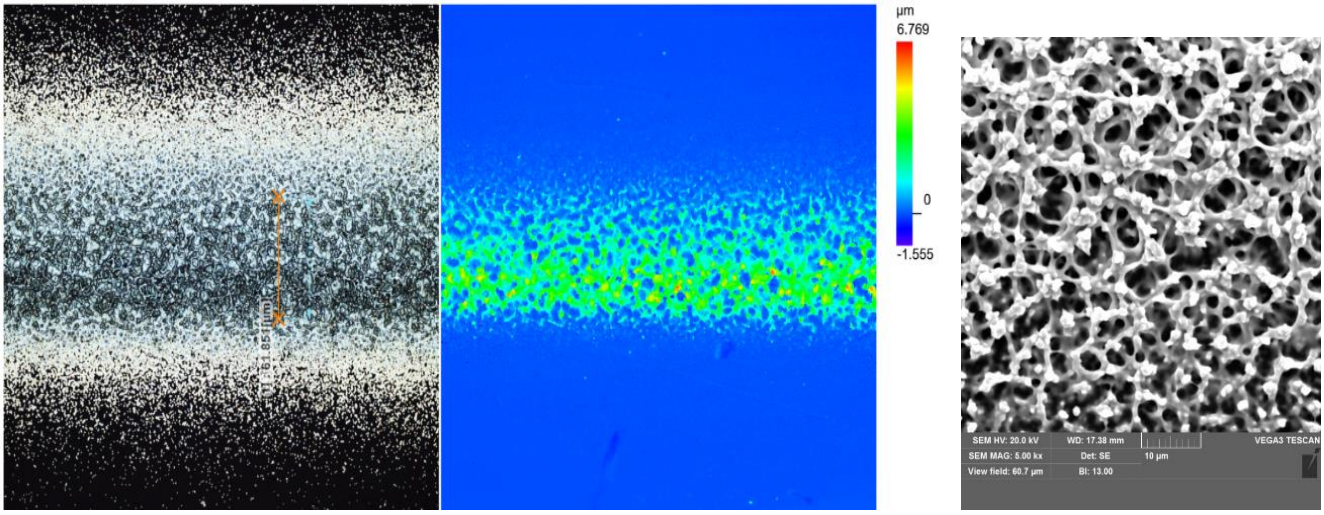

Fig. 14. DM micrograph of the trace surface printed with insufficient aerosol volume, sample (a) with CM scan along marked transverse line (b) and SEM image (SE) in the middle of trace width (c).

3.4. Infrared sintering

The same printed samples were sintered by IR lamp. NIR dot lamp heated only printed lines instead of whole foil samples. The sintering time was 5 min and 2.5 min, for a traverse speed of 10 mm/min and 20 mm/min, respectively. Regardless of the speed of sintering, the quality of the samples depended on the printing process. Intensive open porosity was present in traces printed without substrate heating (Fig. 15a). Sample IR 1 sintered with lower traverse speed generates a finer structure with bonded particles and visible aggregates (Fig. 15b). In the case of sample IR 2 single aggregates can be distinguished in the standard topography mode (Fig. 15c) and were highlighted by phase image which is relative to sample material contrast (Fig. 15d). Smoother surface structure of IR 1 sample arises from higher thermal energy generated while sintering with lower traverse speed. The energy was sufficient to bond all aggregates to solid material. It should be noted that without substrate heating, the trace material contains residues of the liquid phase and polymer material, which have to be removed and restrain the short-time sintering.

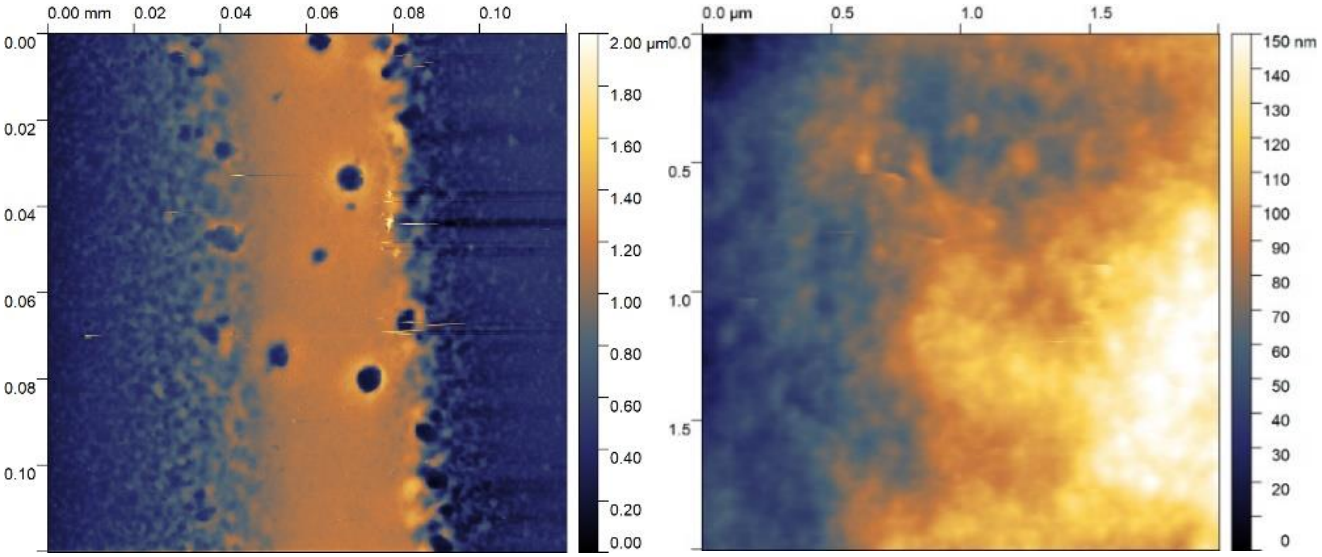

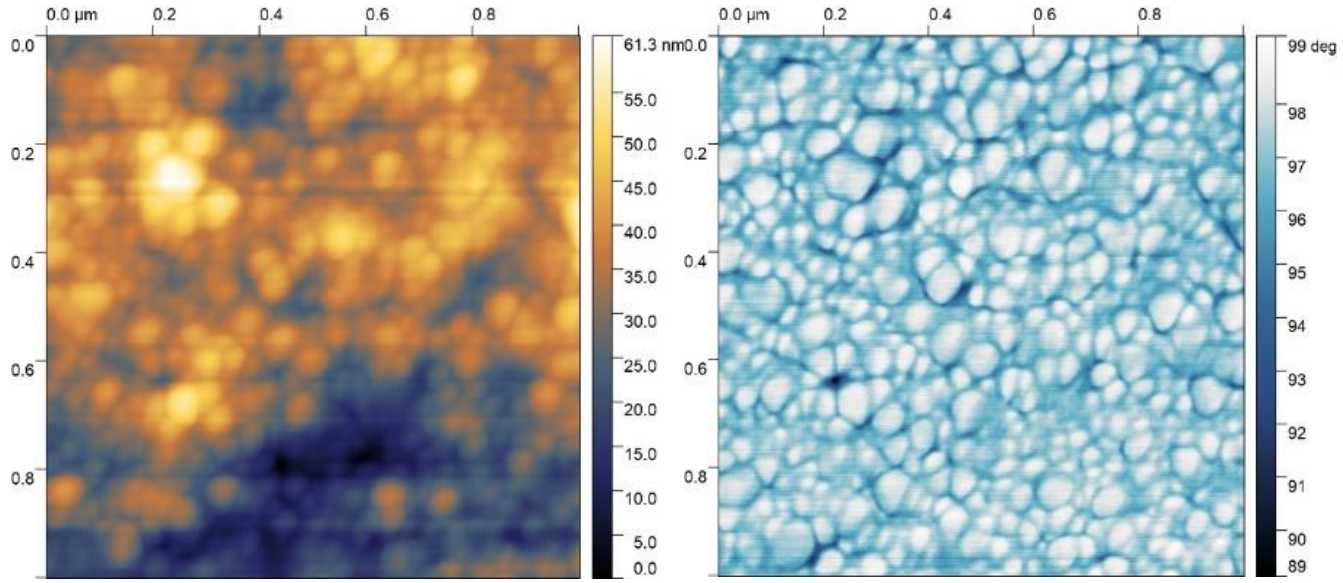

Fig. 15. AFM scans of sample IR 1 (a,b) and IR 2 (c,d). Topography (a-c) and topography phase image - relative to sample material (d)

Substrate heating enhanced liquid evaporation and aerosol deposition. Samples IR1+H and IR2+H showed excessive development of overspray in the trace boundary region. Figure 16 presents a set of peaks in the overspray area that are higher even than the main part of the trace. Independently of the traverse speed, IR sintering in combination with substrate heating in the printing process provided a continuous and smooth surface of the trace. In comparison to the AP+H sample (Fig. 17), the smoothing effect of the sintered samples is clearly visible. Agglomerates bound by liquid residues form a wavy surface topography. AFM in the phase image (Fig. 17c) confirmed a slack structure without the presence of solid material. On the contrary, single silver particles were detected in IR1+H sample by high resolution AFM topography scans, which are particularly visible in friction mode (Fig. 18). Large sintered aggregates with clear boundary lines in the pits consist of many fine silver particles. Therefore, it is stated that drying process form loosely bound particles in agglomerates, while the sintering process can be divided into two steps. In the first step, the particles inside the agglomerates are bonded, forming aggregates, and in the second step, the aggregates are joined together. Comparison of the roughness of the sintered prints on nano-scale (see Tab. 5) shows that the elongated time of the sintering, independently of the heating source, provides more thermal energy and consequently minimises the surface roughness from Sa 821 nm to 16 nm for the AP+H and IR1 samples, respectively. However, the roughness of samples printed with substrate heating is slightly higher, probably due to increased half-dried aerosol deposition with lowered viscosity.

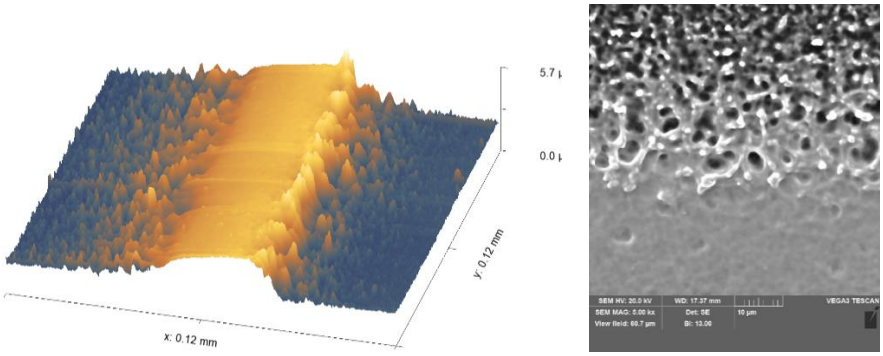

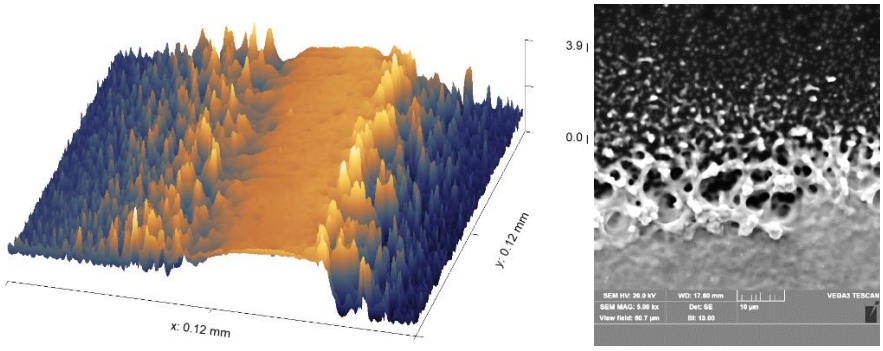

Fig. 16. AFM topography images (a,c) and SEM-SE micrographs (b,d) of IR1+H (a,b) and IR2+H (c,d).

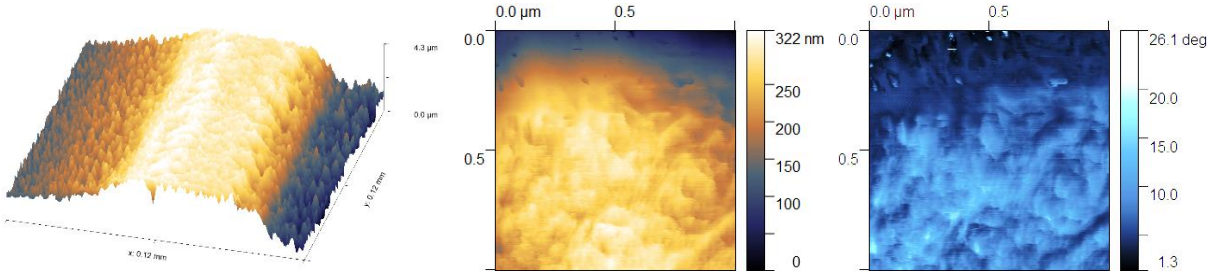

Fig. 17. AFM topography image (a,b) and phase image (c) scans of AP+H sample.

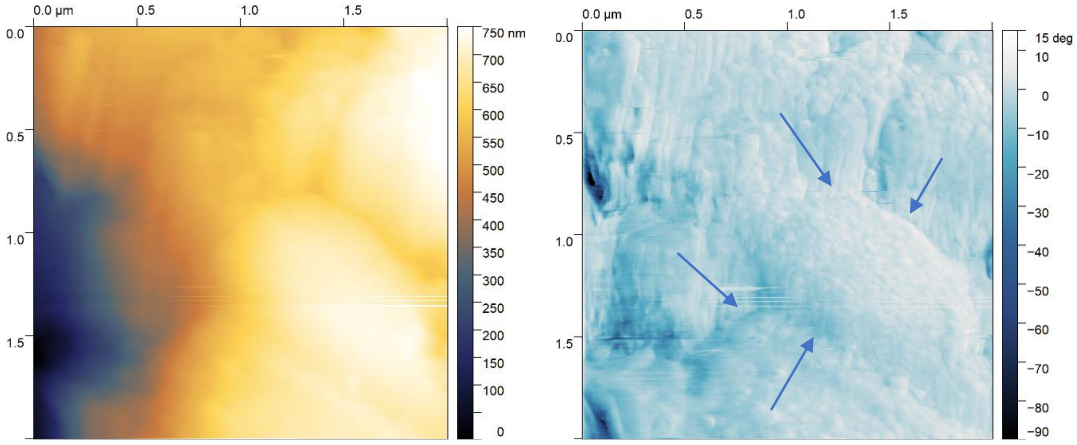

Fig. 18. High resolution AFM topography image (a) and friction mode – LF (b) of IR1+H sample. Blue arrows indicate the boundary lines between sintered aggregates.

4. Discussion

The most troublesome issue in AJP is the overspray formed usually in the nearest region of the printed trace. In some cases, the spattered overspray can cover tens of square millimetres of the substrate. It results from the presence of small aerosol droplets below 1 µm [22]. Fine droplets are ejected from the main stream and create an aerosol cloud that electrostatically embed on the foil. Skarżyński et al. [57] concluded that wider overspray and lesser homogeneity of the trace result from lower Saffman force acting on fine aerosol droplets. The problem firstly was solved by adding virtual impactor to the line transporting ink aerosol to separate fine droplets [67],[52]. However, this solution increases the costs of the process by intensifying ink consumption. The present study showed that overspray can be limited and aerosol cloud spatter totally eliminated by applying heating of the bed, which significantly influences the properties of the ink. As a silver nanoparticles suspension, the ink has to be chemically stabilised and therefore contains a precise mixture of surfactants, polymer additives, and solvent [44]. All of the stabilisers are temperature sensitive. Therefore, the printing nozzle is usually fixed close to the substrate to increase control of the process. However, with activated bed heating, the temperature is transferred to the nozzle, enhancing evaporation of the solvent directly in the stream. As a consequence, the properties of the ink change, the

surface tension decreases [4], while the viscosity and density increases, facilitating the deposition [69]. It should be emphasised that the alcohol and polymer additives to the ink are responsible for controllable transport of nanosized silver particles. Nevertheless, after deposition, the solvent has to be removed to bond metal particles into a solid continuous trace. Heating of the bed helps to accelerate the drying process by promoting the evaporation of solvents and leads to changes in the concentration due to destabilization of surfactants [19],[30]. This prevents the formation of defects and allows for faster printing speeds. However, heating of the deposited ink in the trace starts the decomposition of the silver precursor at the temperature above the boiling point and the decay temperature of the solvent. Therefore, silver nanoparticles are bound and form agglomerates [70] in situ in the absence of solvent (Fig. 17) or clusters [29], when a small number of nanoparticles are attached to aerosol droplets (see Fig. 16b,d). The clusters are formed by polymerisation of the capillary bridges in the wet state, at moderate temperatures below 100 °C [21]. Pham-Van et al. [50] hypothesised that these clusters form structures that minimise the second moment of mass distribution. Moreover, Yang et al. [70] stated that thermal decomposition of the ink complex would be largely restricted in isolated clusters and as a result form a discontinuous film. The drying process affects polymer solutions, which exhibit a change in surface tension dependent on the local solute concentration and lead to gelation [59],[26]. On the other hand, variations in surface tension along the liquid−gas interface induce a Marangoni flow that pushes particles away from the contact line and therefore leads to suppression of the CRE [4]. Anyfantakis et al. [5] reported that suspension surfactants are responsible for solutal Marangoni flow and flattening of the profile of the final polymer film. This phenomenon was observed in present study by formation of porous overspray. What is more, these porous features of solidifying suspension can also be attributed to the breakdown of planar growth due to instability of the solid–liquid interface. These factors influence growth kinetics and determine the growth morphology [45].

After printing, the sintering process begins and is usually divided into two stages. In the first stage, the nanoparticles in the agglomerates are bonded to the solid material. However, the residue of the chemical stabilisers provides an energy barrier to sintering. Therefore, the removal of stabilizers typically requires a temperature higher than 250 °C and a relatively long time due to a relatively large amount of surface residues (>10 wt.%) [41], low mobility and physical adsorption of surfactants [72]. It should be noted that thermal energy requirements are reduced in the area of agglomerates due to the action of surface energy and van der Waals forces between nanoparticles [32],[17],[7]. In the second stage, the sintered aggregates are joined together, forming a solid trace (Fig. 18). The sintering of AP samples printed without bed heating results in a finer material structure (see Fig. 15) due to possible particles migration while sintering, which was confirmed by nano-scale roughness measurement. However, the structure shows some porosity and non-continuity between aggregates with possibility to microcracks generation. Gramlich et al. [16] found that sintering should begin before the film is fully dried to form sintering necks and increase the particle-to-particle bonding significantly above the previously predominant van der Waals force. As a result, sintered material can resist capillary pressure and thereby prevent cracks.

The selection of the sintering method and the sintering parameters significantly affected the quality of the prints. The furnace sintering lasts much longer, and the entire substrate is heated uniformly. On the contrary, infrared radiation directly affected the traces by penetrating the printed layer, causing localised heating and enabling selective sintering of the material. While infrared sintering can provide rapid heating, precise temperature control might be more challenging than in furnace. On the other hand, some heat-sensitive substrates may be unsuitable for furnace sintering due to prolonged exposure to high temperatures. Therefore, IR sintering is more suitable for heat sensitive substrates, as it provides localised heating without subjecting the entire substrate to prolonged affection of high temperatures [63],[18]. The results showed that furnace sintering (FS) without bed heating in 1 hour generated high nano-porosity due to insufficient energy. Increasing the sintering time to 2 hours solved the problem, the porosity faded (compare Fig. 10 and Fig. 11) and roughness decreased (Tab.5). The quality of the prints was verified by resistance measurements. Defects detected in samples FS1 and FS1+H were responsible for the highest values of sheet resistance. Extended time decreased twice order of magnitude from 29.6

Ω/□ to 0.283 Ω/□ in sample FS1 and FS2, respectively. In the case of infrared sintering, the traverse velocity of the polymer substrate regulated the material structure. The lower velocity applied in samples IR1 and IR1+H provided much lower nano-scale roughness (Tab. 5), indicating decreasing of porosity. As a result, a decrease in a sheet resistance was achieved.

It should be emphasised that the sheet resistance of the printed traces is comparable with the results obtained for commercially available printers. Chen et al. [12] printed large traces of 2 mm width and 10 μm thick on paper substrate and obtained a sheet resistance of 1.13×10^{-2} Ω/□, while Seiti et al. [55] declared a sheet resistance in the range of 0.05-0.1 Ω/□ on polymer substrate, depending on the ink and trace geometry. The prints fabricated in this study and sintered by IR lamp fall within the range. Nevertheless, additional in-line bed heating should be applied to increase the thickness of the prints and as a result decrease resistance.

5. Conclusions

In the presented study, silver-nanoparticle based ink was applied in aerosol jet printing process to fabricate prints on flexible polyimide substrates. Samples were prepared without or with additional in-line heating of the substrate material to temperature of 90 ˚C. The major problem of the process is the formation of the spatter. Fine droplets with diameter below 1 μm are ejected from the stream and create aerosol cloud that electrostatically embed on the foil. An additional problem was the local open porosity that resulted from evaporation of the solvent. A gas formed inside the trace from the drying liquid exerted pressure, leaving open porosities in the central continuous part of the prints that resemble ‘chimneys’. The present study showed that overspray can be limited, while aerosol cloud spatter and open porosity are totally eliminated, by applying bed heating. The heat transferred to the nozzle increases the viscosity and density of the ink due to accelerated evaporation of the solvent from the aerosol. As a consequence, the agglomerates with increased nanoparticles concentration prevent defect formation. Furthermore, the enhanced deposition of silver nanoparticles increases the thickness of the traces.

All printed samples were sintered in furnace at 230 ˚C for 60 min or 120 min or by IR lamp with a voltage of 5 V and a traverse velocity of 10 or 20 mm/min. The sintering parameters recommended by the ink manufacturer, i.e., furnace heating at 230 ˚C for 60 min were insufficient, generating defined by AFM nano-porosity and high roughness. Increasing the sintering time to 120 min smoothed the surface of the trace by decreasing porosity and roughness as well. In the case of IR sintering, the material structure was regulated by the process traverse velocity, and thus samples sintered with a lower velocity showed the lowest nanoscale roughness, indicating the smoothest sample surface.

The use of infrared light for sintering aerosol jet printed traces offers several advantages. It allows for rapid and localised heating, enabling precise control over the sintering process. Infrared sintering also reduces the thermal impact on the surrounding materials, minimising the risk of damage to the substrate. Additionally, the process can be easily integrated into existing manufacturing lines or combined with printer, making a practical solution for large-scale production of electronic devices. The research confirmed that properly planned AJP process improves the quality and reliability of the printed traces.

Acknowledgments

This work was funded by The National Centre for Research and Development [LIDER/42/0142/L-11/19/NCBR/2020] (Project title: Sonic Jet – precise printer for manufacturing elastic electronics).

References

1. Agarwala S, Goh G L, Yeong W Y. Optimizing aerosol jet printing process of silver ink for printed electronics. IOP Conference Series: Materials Science and Engineering 2017; 191(1): 012027, https://doi.org/10.1088/1757-899X/191/1/012027.
2. Al-Halhouli A, Qitouqa H, Alashqar A, Abu-Khalaf J. Inkjet printing for the fabrication of flexible/stretchable wearable electronic devices and sensors. Sensor Review 2018; 38(4): 438–452, https://doi.org/10.1108/SR-07-2017-0126.
3. Andritsos K, Theodorakos I, Zacharatos F et al. Conformal laser printing and laser sintering of Ag nanoparticle inks: a digital approach for the additive manufacturing of micro-conductive patterns on patterned flexible substrates. Virtual and Physical Prototyping 2023; 18(1): e2138462, https://doi.org/10.1080/17452759.2022.2138462.

4. Anyfantakis M, Geng Z, Morel M et al. Modulation of the Coffee-Ring Effect in Particle/Surfactant Mixtures: the Importance of Particle–Interface Interactions. Langmuir 2015; 31(14): 4113–4120, https://doi.org/10.1021/acs.langmuir.5b00453.
5. Anyfantakis M, Geng Z, Morel M et al. Modulation of the Coffee-Ring Effect in Particle/Surfactant Mixtures: the Importance of Particle–Interface Interactions. Langmuir 2015; 31(14): 4113–4120, https://doi.org/10.1021/acs.langmuir.5b00453.
6. Arsenov P V, Efimov A A, Ivanov V V. Comparison of Thermal and Electrical Sintering of Aerosol Silver Nanoparticles in Process of Aerosol Jet Printing. Key Engineering Materials 2020; 834: 10–15, https://doi.org/10.4028/www.scientific.net/KEM.834.10.
7. Bahadur N M, Furusawa T, Sato M et al. Fast and facile synthesis of silica coated silver nanoparticles by microwave irradiation. Journal of Colloid and Interface Science 2011; 355(2): 312–320, https://doi.org/10.1016/j.jcis.2010.12.016.
8. Bandodkar A J, Jeerapan I, You J-M et al. Highly Stretchable Fully-Printed CNT-Based Electrochemical Sensors and Biofuel Cells: Combining Intrinsic and Design-Induced Stretchability. Nano Letters 2016; 16(1): 721–727, https://doi.org/10.1021/acs.nanolett.5b04549.
9. Beedasy V, Smith P J. Printed Electronics as Prepared by Inkjet Printing. Materials 2020; 13(3): 704, https://doi.org/10.3390/ma13030704.
10. Caputo D, de Cesare G, Lo Vecchio N et al. Polydimethylsiloxane material as hydrophobic and insulating layer in electrowetting-on-dielectric systems. Microelectronics Journal 2014; 45(12): 1684–1690, https://doi.org/10.1016/j.mejo.2014.05.016.
11. Chen H, Dai F, Hu M et al. Heat-resistant polyimides with low CTE and water absorption through hydrogen bonding interactions. Journal of Polymer Science 2021; 59(17): 1942–1951, https://doi.org/10.1002/pol.20210305.
12. Chen Y-D, Nagarajan V, Rosen D W et al. Aerosol jet printing on paper substrate with conductive silver nano material. Journal of Manufacturing Processes 2020; 58: 55–66, https://doi.org/10.1016/j.jmapro.2020.07.064.
13. Chen Y-D, Nagarajan V, Rosen D W et al. Aerosol jet printing on paper substrate with conductive silver nano material. Journal of Manufacturing Processes 2020; 58: 55–66, https://doi.org/10.1016/j.jmapro.2020.07.064.
14. Das R, Nath S S, Chakdar D et al. Synthesis of silver nanoparticles and their optical properties. Journal of Experimental Nanoscience 2010; 5(4): 357–362, https://doi.org/10.1080/17458080903583915.
15. Fu L-M, Hsu J-H, Shih M-K et al. Process Optimization of Silver Nanoparticle Synthesis and Its Application in Mercury Detection. Micromachines 2021; 12(9): 1123, https://doi.org/10.3390/mi12091123.
16. Gramlich G, Huber R, Häslich F et al. Process considerations for Aerosol-Jet printing of ultra fine features. Flexible and Printed Electronics 2023; 8(3): 035002, https://doi.org/10.1088/2058-8585/ace3d8.
17. Granbohm H, Larismaa J, Ali S et al. Control of the Size of Silver Nanoparticles and Release of Silver in Heat Treated SiO2-Ag Composite Powders. Materials 2018; 11(1): 80, https://doi.org/10.3390/ma11010080.
18. Gu W, Yuan W, Zhong T et al. Fast near infrared sintering of silver nanoparticle ink and applications for flexible hybrid circuits. RSC Advances 2018; 8(53): 30215–30222, https://doi.org/10.1039/C8RA04468F.
19. Halonen E, Viiru T, Ostman K et al. Oven Sintering Process Optimization for Inkjet-Printed Ag Nanoparticle Ink. IEEE Transactions on Components, Packaging and Manufacturing Technology 2013; 3(2): 350–356, https://doi.org/10.1109/TCPMT.2012.2226458.
20. Hassan G, Bae J, Lee C H. Ink-jet printed transparent and flexible electrodes based on silver nanoparticles. Journal of Materials Science: Materials in Electronics 2018; 29(1): 49–55, https://doi.org/10.1007/s10854-017-7886-2.
21. Hauf K, Koos E. Structure of capillary suspensions and their versatile applications in the creation of smart materials. MRS Communications 2018; 8(2): 332–342, https://doi.org/10.1557/mrc.2018.28.
22. Hoey J M, Lutfurakhmanov A, Schulz D L, Akhatov I S. A Review on Aerosol-Based Direct-Write and Its Applications for Microelectronics. Journal of Nanotechnology 2012; 2012: e324380, https://doi.org/10.1155/2012/324380.
23. Ivanišević I, Kassal P, Milinković A et al. Combined Chemical and Thermal Sintering for High Conductivity Inkjet-printed Silver Nanoink on Flexible Substrates. Chemical & biochemical engineering quarterly 2019; 33(3): 377–384, https://doi.org/10.15255/CABEQ.2019.1585.
24. Jiao L, Du Z, Dai X et al. Multifunctional polyimide films with superheat-resistance, low coefficient of thermal expansion and fluorescence performance. Polymer 2022; 247: 124792, https://doi.org/10.1016/j.polymer.2022.124792.
25. Jiao L, Luo F, Du Z et al. Ultra-high Tg and ultra-low CTE polyimide films based on tunable interchain crosslinking. Reactive and Functional Polymers 2022; 181: 105449, https://doi.org/10.1016/j.reactfunctpolym.2022.105449.
26. Kajzer W, Jaworska J, Jelonek K et al. Corrosion resistance of Ti6Al4V alloy coated with caprolactone-based biodegradable polymeric coatings. Eksploatacja i Niezawodność – Maintenance and Reliability 2018; 20(1): 30–38, https://doi.org/10.17531/ein.2018.1.5.

27. Kang J S, Ryu J, Kim H S, Hahn H T. Sintering of Inkjet-Printed Silver Nanoparticles at Room Temperature Using Intense Pulsed Light. Journal of Electronic Materials 2011; 40(11): 2268–2277, https://doi.org/10.1007/s11664-011-1711-0.
28. Keller D J, Jochem K S, Suszynski W J, Francis L F. Near-IR sintering of conductive silver nanoparticle ink with in situ resistance measurement. Journal of Coatings Technology and Research 2019; 16(6): 1699–1705, https://doi.org/10.1007/s11998-019-00268-5.
29. Koos E. Capillary suspensions: Particle networks formed through the capillary force. Current Opinion in Colloid & Interface Science 2014; 19(6): 575–584, https://doi.org/10.1016/j.cocis.2014.10.004.
30. Kotnarowska D, Żabińska A. Influence of aqueous sodium chloride solutions on operational properties of epoxy coatings. Eksploatacja i Niezawodność – Maintenance and Reliability 2022; 24(4): 629–640, https://doi.org/10.17531/ein.2022.4.4.
31. Krzeminski J, Blicharz B, Skalski A et al. Photonic curing of silver paths on 3D printed polymer substrate. Circuit World 2019; 45(1): 9–14, https://doi.org/10.1108/CW-11-2018-0084.
32. Kulkarni P, Baron P A, Willeke K. Introduction to Aerosol Characterization. Aerosol Measurement, John Wiley & Sons, Ltd: 2011: 1–13, https://doi.org/10.1002/9781118001684.ch1.
33. Kumar R, Shin J, Yin L et al. All-Printed, Stretchable Zn-Ag2O Rechargeable Battery via Hyperelastic Binder for Self-Powering Wearable Electronics. Advanced Energy Materials 2017; 7(8): 1602096, https://doi.org/10.1002/aenm.201602096.
34. Lapa W, Winnicki M, Orłowska K. Investigation of aerosol droplets diameter generated in aerosol jet printing. Materials Science-Poland 2022; 40(4): 78–90, https://doi.org/10.2478/msp-2022-0046.
35. Laurent Ph, Stoukatch S, Dupont F, Kraft M. Electrical characterization of Aerosol Jet Printing (AJP) deposited conductive silver tracks on organic materials. Microelectronic Engineering 2018; 197: 67–75, https://doi.org/10.1016/j.mee.2018.06.002.
36. Liang S, Liu J. Colorful liquid metal printed electronics. Science China Technological Sciences 2018; 61(1): 110–116, https://doi.org/10.1007/s11431-017-9116-9.
37. Lin W-H, Ouyang F-Y. Electromigration Behavior of Screen-Printing Silver Nanoparticles Interconnects. JOM 2019; 71(9): 3084–3093, https://doi.org/10.1007/s11837-019-03627-0.
38. Lopes A J, Lee I H, MacDonald E et al. Laser curing of silver-based conductive inks for in situ 3D structural electronics fabrication in stereolithography. Journal of Materials Processing Technology 2014; 214(9): 1935–1945, https://doi.org/10.1016/j.jmatprotec.2014.04.009.
39. Lopes A J, MacDonald E, Wicker R B. Integrating stereolithography and direct print technologies for 3D structural electronics fabrication. Rapid Prototyping Journal 2012; 18(2): 129–143, https://doi.org/10.1108/13552541211212113.
40. Lukacs P, Pietrikova A, Cabuk P. Dependence of electrical resistivity on sintering conditions of silver layers printed by InkJet printing technology. Circuit World 2017; 43(2): 80–87, https://doi.org/10.1108/CW-02-2017-0008.
41. Mavuri A, Mayes A G, Alexander M S. Inkjet Printing of Polyacrylic Acid-Coated Silver Nanoparticle Ink onto Paper with Sub-100 Micron Pixel Size. Materials 2019; 12(14): 2277, https://doi.org/10.3390/ma12142277.
42. McKibben N, Ryel B, Manzi J et al. Aerosol jet printing of piezoelectric surface acoustic wave thermometer. Microsystems & Nanoengineering 2023; 9(1): 1–12, https://doi.org/10.1038/s41378-023-00492-5.
43. Mo L, Guo Z, Yang L et al. Silver Nanoparticles Based Ink with Moderate Sintering in Flexible and Printed Electronics. International Journal of Molecular Sciences 2019; 20(9): 2124, https://doi.org/10.3390/ijms20092124.
44. Mościcki A, Smolarek-Nowak A, Felba J, Kinart A. Ink for Ink-Jet Printing of Electrically Conductive Structures on Flexible Substrates with Low Thermal Resistance. Journal of Electronic Materials 2017; 46(7): 4100–4108, https://doi.org/10.1007/s11664-017-5320-4.
45. Naviroj M, Voorhees P W, Faber K T. Suspension- and solution-based freeze casting for porous ceramics. Journal of Materials Research 2017; 32(17): 3372–3382, https://doi.org/10.1557/jmr.2017.133.
46. Nguyen P Q M, Yeo L-P, Lok B-K, Lam Y-C. Patterned Surface with Controllable Wettability for Inkjet Printing of Flexible Printed Electronics. ACS Applied Materials & Interfaces 2014; 6(6): 4011–4016, https://doi.org/10.1021/am4054546.
47. Park J, Kang H J, Shin K-H, Kang H. Fast sintering of silver nanoparticle and flake layers by infrared module assistance in large area roll-to-roll gravure printing system. Scientific Reports 2016; 6(1): 34470, https://doi.org/10.1038/srep34470.
48. Park J D, Lim S, Kim H. Patterned silver nanowires using the gravure printing process for flexible applications. Thin Solid Films 2015; 586: 70–75, https://doi.org/10.1016/j.tsf.2015.04.055.
49. Parupelli S K, Desai S. Hybrid additive manufacturing (3D printing) and characterization of functionally gradient materials via in situ laser

curing. The International Journal of Advanced Manufacturing Technology 2020; 110(1): 543–556, https://doi.org/10.1007/s00170-020-05884-9.

50. Pham-Van H, Tran-Phan-Thuy L, Tran-Manh C et al. Two-Dimensional Clusters of Colloidal Particles Induced by Emulsion Droplet Evaporation. Nanomaterials 2020; 10(1): 156, https://doi.org/10.3390/nano10010156.
51. Polzinger B, Schoen F, Matic V et al. UV-sintering of inkjet-printed conductive silver tracks. 2011 11th IEEE International Conference on Nanotechnology, 2011: 201–204, https://doi.org/10.1109/NANO.2011.6144541.
52. Reitelshöfer S, Göttler M, Schmidt P et al. Aerosol-Jet-Printing silicone layers and electrodes for stacked dielectric elastomer actuators in one processing device. Electroactive Polymer Actuators and Devices (EAPAD) 2016, SPIE: 2016; 9798: 350–358, https://doi.org/10.1117/12.2219226.
53. Saleh E, Zhang F, He Y et al. 3D Inkjet Printing of Electronics Using UV Conversion. Advanced Materials Technologies 2017; 2(10): 1700134, https://doi.org/10.1002/admt.201700134.
54. Seifert T, Baum M, Roscher F et al. Aerosol Jet Printing of Nano Particle Based Electrical Chip Interconnects. Materials Today: Proceedings 2015; 2(8): 4262–4271, https://doi.org/10.1016/j.matpr.2015.09.012.
55. Seiti M, Degryse O, Ferraris E. Aerosol Jet® printing 3D capabilities for metal and polymeric inks. Materials Today: Proceedings 2022; 70: 38–44, https://doi.org/10.1016/j.matpr.2022.08.488.
56. Sharif A, Farid N, O'Connor G M. Ultrashort laser sintering of metal nanoparticles: A review. Results in Engineering 2022; 16: 100731, https://doi.org/10.1016/j.rineng.2022.100731.
57. Skarżyński K, Krzemiński J, Jakubowska M, Słoma M. Highly conductive electronics circuits from aerosol jet printed silver inks. Scientific Reports 2021; 11(1): 18141, https://doi.org/10.1038/s41598-021-97312-5.
58. Sreenilayam S P, McCarthy É, McKeon L et al. Additive-free silver nanoparticle ink development using flow-based Laser Ablation Synthesis in Solution and Aerosol Jet printing. Chemical Engineering Journal 2022; 449: 137817, https://doi.org/10.1016/j.cej.2022.137817.
59. Still T, Yunker P J, Yodh A G. Surfactant-Induced Marangoni Eddies Alter the Coffee-Rings of Evaporating Colloidal Drops. Langmuir 2012; 28(11): 4984–4988, https://doi.org/10.1021/la204928m.
60. Suhaimi M I, Nordin A N, Ralib A A M et al. Mechanical durability of screen-printed flexible silver traces for wearable devices. Sensing and Bio-Sensing Research 2022; 38: 100537, https://doi.org/10.1016/j.sbsr.2022.100537.
61. Sung K-H, Park J, Kang H. Multi-Layer Inkjet Printing of Ag Nanoparticle Inks and Its Sintering with a Near-Infrared System. International Journal of Precision Engineering and Manufacturing 2018; 19(2): 303–307, https://doi.org/10.1007/s12541-018-0037-8.
62. Taccola S, da Veiga T, Chandler J H et al. Micro-scale aerosol jet printing of superparamagnetic Fe3O4 nanoparticle patterns. Scientific Reports 2022; 12(1): 1–12, https://doi.org/10.1038/s41598-022-22312-y.
63. Tobjörk D, Aarnio H, Pulkkinen P et al. IR-sintering of ink-jet printed metal-nanoparticles on paper. Thin Solid Films 2012; 520(7): 2949–2955, https://doi.org/10.1016/j.tsf.2011.10.017.
64. Vaithilingam J, Saleh E, Körner L et al. 3-Dimensional inkjet printing of macro structures from silver nanoparticles. Materials & Design 2018; 139: 81–88, https://doi.org/10.1016/j.matdes.2017.10.070.
65. Vandevenne G, Marchal W, Verboven I et al. A study on the thermal sintering process of silver nanoparticle inkjet inks to achieve smooth and highly conducting silver layers. physica status solidi (a) 2016; 213(6): 1403–1409, https://doi.org/10.1002/pssa.201533007.
66. Werner C, Godlinski D, Zöllmer V, Busse M. Morphological influences on the electrical sintering process of Aerosol Jet and Ink Jet printed silver microstructures. Journal of Materials Science: Materials in Electronics 2013; 24(11): 4367–4377, https://doi.org/10.1007/s10854-013-1412-y.
67. Wilkinson N J, Smith M A A, Kay R W, Harris R A. A review of aerosol jet printing—a non-traditional hybrid process for micro-manufacturing. The International Journal of Advanced Manufacturing Technology 2019; 105(11): 4599–4619, https://doi.org/10.1007/s00170-019-03438-2.
68. Wu K, Hong J, Qi X et al. Screen printing of silver nanoparticles on the source/drain electrodes of organic thin-film transistors. Organic Electronics 2022; 106: 106524, https://doi.org/10.1016/j.orgel.2022.106524.
69. Xiaoru Pan, Li D, Guo M et al. Densities and Viscosities of N,N-Dimethylaniline and Mixtures with Methanol, Ethanol, 1-Propanol, and

1-Butanol at 298.15–313.15 K. Russian Journal of Physical Chemistry A 2019; 93(9): 1715–1721, https://doi.org/10.1134/S0036024419090309.

70. Yang W, Wang C, Arrighi V. An organic silver complex conductive ink using both decomposition and self-reduction mechanisms in film formation. Journal of Materials Science: Materials in Electronics 2018; 29(4): 2771–2783, https://doi.org/10.1007/s10854-017-8205-7.
71. Yu Z, Huang F, Zhang T et al. Effects of different thermal sintering temperatures on pattern resistivity of printed silver ink with multiple particle sizes. AIP Advances 2021; 11(11): 115116, https://doi.org/10.1063/5.0067651.
72. Zhang R, Lin W, Moon K, Wong C P. Fast Preparation of Printable Highly Conductive Polymer Nanocomposites by Thermal Decomposition of Silver Carboxylate and Sintering of Silver Nanoparticles. ACS Applied Materials & Interfaces 2010; 2(9): 2637–2645, https://doi.org/10.1021/am100456m.
73. https://amepox-mc.pl/ (accessed 23 November 2023).